



Photonic spiking neural network based on excitable VCSELs-SA for sound azimuth detection

ZI WEI SONG,¹ SHUI YING XIANG,^{1,2,*} ZHEN XING REN,¹ SU HONG WANG,¹ AI JUN WEN,¹ AND YUE HAO²

¹State Key Laboratory of Integrated Service Networks, Xidian University, Xi'an 710071, China

²State Key Discipline Laboratory of Wide Bandgap Semiconductor Technology, School of Microelectronics, Xidian University, Xi'an 710071, China

*jxxy@126.com

Abstract: We propose a photonic spiking neural network (SNN) based on excitable vertical-cavity surface-emitting lasers with an embedded saturable absorber (VCSELs-SA) for emulating the sound azimuth detection function of the brain for the first time. Here, the spike encoding and response properties based on the excitability of VCSELs-SA are employed, and the difference between spike timings of two postsynaptic neurons serves as an indication of sound azimuth. Furthermore, the weight matrix contributing to the successful sound azimuth detection is carefully identified, and the effect of the time interval between two presynaptic spikes is considered. It is found that the weight range that can achieve sound azimuth detection decreases gradually with the increase of the time interval between the sound arriving at the left and right ears. Besides, the effective detection range of the time interval between two presynaptic spikes is also identified, which is similar to that of the biological auditory system, but with a much higher resolution which is at the nanosecond time scale. We further discuss the effect of device variations on the photonic sound azimuth detection. Hence, this photonic SNN is biologically plausible, which has comparable low energy consumption and higher resolution compared with the biological system. This work is valuable for brain-inspired information processing and a promising foundation for more complex spiking information processing implemented by photonic neuromorphic computing systems.

© 2020 Optical Society of America under the terms of the [OSA Open Access Publishing Agreement](#)

1. Introduction

The brain network is a highly complex and ordered network that integrates various stimuli from the sensory units and responds to these stimuli. The powerful computing capability of the brain is due to the fact that numerous neurons form a complex neural network through synapses connection, so core computational units of every neural network are neurons and synapses [1,2]. Artificial neural networks, which aim to explore effective solutions for complex neural activities by establishing corresponding neural computing models and system principles, have attracted extensive attention and acquired very wide applications [3]. As the third generation of artificial neural networks computing model, spiking neural networks (SNNs) are more biologically plausible, hardware friendly and energy-efficient than the conventional artificial neural networks [4,5]. The SNN processes information in a way which is more analogous to the brain, since it consists of spiking neuron models [6] regarded as basic units. More precisely, information is represented and processed by the precise timing of spiking sequences.

In recent years, many neural computing functions have gained great progresses with the electronic neuromorphic computing techniques [7–23]. However, different drawbacks exist in the forms of energy-efficiency and speed for these approaches. Photonic neuromorphic computing, which is an emerging interdisciplinary field combining the advantages of both optical techniques

and neuromorphic computing, offers an alternative approach to implement SNNs, but is still in its infancy. Compared with the electronic counterparts, photonic neuromorphic computing shows promise in both the advantages of low power consumption and high speed. With the joint efforts of the researchers all over the world, the photonics-based neuromorphic computing shows advancement in implementations of various kinds of neural processing units on the photonic platform, including various photonic neurons [24–40], photonic synapses [41–48], and photonic neuromorphic systems [28,30–32,49]. In recently proposed photonic neuromorphic platforms, vertical-cavity surface-emitting lasers (VCSELs) which exhibit advantages of low manufacturing cost, easy to integrate into two-dimensional arrays, and high energy efficiency, have been widely served as photonic neurons [24,26,28,33–39]. Hurtado *et al.* proposed that VCSELs can be employed as artificial neuron models in 2010 [24]. They also investigated experimentally and theoretically the controllable excitation and inhibition of spiking dynamics to replicate various biological neuronal responses [26,34–36]. The group of Prucnal proved for the first time that a VCSEL with an embedded saturable absorber (VCSEL-SA) could mimic an excitable leaky integrate-and-fire (LIF) neuron. Furthermore, they derived the theoretical model of the excitable VCSEL-SA based on the well-known Yamada model [28], which plays the foundation role for the preliminary numerical demonstration of various photonic neural computing functions based on photonic SNN consisting of VCSELs-SA. However, there are still many pain points in the field of photonic neuromorphic computing, which range from the chip, device, system, network, algorithm, as well as the application from both theoretical and experimental aspects. Even the feasibility and workability of neural computing function with the photonic neuromorphic computing techniques remain largely unexplored, which deserve further exploration so as to fill the gap between electronic and photonic neuromorphic computing.

Sound azimuth detection is an important function collaboratively performed by the brain and ears, allowing an awareness of the environment and permitting animals to locate prey [50]. In recent years, there have been many SNNs based on different devices that can realize sound azimuth detection function in the electrical domain. For instance, Wang *et al.* demonstrated that an electronic neuromorphic network based on resistive random-access memories was capable of mimicking the detection of sound azimuth by the brain [21]. In that network, the difference between the internal potentials of two postsynaptic neurons (POSTs) was employed to indicate information about sound direction. He *et al.* proposed a capacitively coupled multiterminal oxide-based neuro-transistors network and successfully demonstrated the workability of sound azimuth detection function with electronic neuromorphic computing platform [51]. In this work, the ratio of the current amplitude of two POSTs was used to indicate the relative timing of the spikes of two presynaptic neurons (PREs) [51]. These approaches operate at similar time scales (at the millisecond time scale) to the biological neural network. However, the workability of sound azimuth detection with photonic platform has not yet been addressed. It is well known that, compared with the neural computing function implemented based on the electrical platform, the sound azimuth detection based on the photonic platform inherently shows the advantages of low power consumption and high resolution (at the nanosecond time scale). Furthermore, the operating condition of the photonic implementation of sound azimuth detection function also deserves further in-depth investigation, which can provide theoretical guidelines for constructing an experimental platform of photonic sound azimuth detection.

In this paper, largely inspired and motivated by Refs. [28] and [51], we propose a photonic SNN consisting of photonic neurons based on excitable VCSELs-SA to emulate sound azimuth detection function of the brain, to the best of our knowledge, for the first time. The main contributions: firstly, the workability of sound azimuth detection with photonic SNN consisting of excitable VCSEL-SA is demonstrated. Secondly, we also reveal the operating conditions required for the successful implementation of photonic sound azimuth detection through extensive numerical simulations. Thirdly, we further discuss the role of device variations on the performance

of sound azimuth detection with the photonic SNN. The photonic SNN processes information by the precise spike timings, which takes advantage of the excitability property in VCSEL-SA neurons. Here, different from the method adopted in Ref. [51], the difference between the precise spike timing of two POSTs is used as an indication of the sound azimuth. Through extensive simulations, the dependence of the difference between the spike timings of two POSTs on the relative timing of the spikes of two PREs is revealed. The rest of this paper is organized as follows. In Section 2, the photonic SNN architecture for mimicking sound azimuth detection of the brain is described. The theoretical model of photonic spiking neurons based on VCSELs-SA is also introduced. Section 3 explores the spike encoding property of PREs and the response property of POSTs based on the excitability of VCSELs-SA, which are essential for performing the sound localization task with the proposed photonic SNN. In Section 4, the implementation of the sound azimuth detection function in this photonic SNN is described in detail. The weight matrix contributing to the successful sound azimuth detection is carefully identified, and the effect of the time interval between two presynaptic spikes on the available synapse weight range is analyzed. Moreover, the effective detection range of the time interval between two presynaptic spikes is also identified. The effects of device variations including different bias currents and transmission delays on the sound azimuth detection performance are also discussed. Finally, conclusions are given in Section 5.

2. Model and theory

2.1. Photonic SNN architecture

The LIF neuron model has a similar response to the biological neuron, which fires a spike when the membrane potential exceeds the threshold value, otherwise it keeps silent [52,53]. The LIF model is the simplest known model for spike processing, and one of the most commonly used spiking neuron models in computational neuroscience [6]. The proposed photonic SNN employs VCSELs-SA as spiking neurons, due to the fact that a VCSEL-SA possessing the excitability property behaves analogously to the LIF model.

Here, we construct a photonic SNN architecture based on excitable VCSELs-SA to mimic the sound azimuth detection of the brain by detecting the precise spike timing difference. The sound azimuth detection function refers to the ability to determine where a sound signal is generated [54]. As shown in Fig. 1(a), the interaural time difference (ITD) [55], which is defined as the difference in arrival times between a sound signal reaching each individual ear, i.e., $ITD = t_L - t_R$, is a predominant binaural cue in the sound azimuth detection of the brain. Here, t_L and t_R represent the times of the sound arriving at the left ear and right ear, respectively. Hence, the direction of sound propagation can be estimated according to the ITD. More precisely, when $ITD > 0$ ($ITD < 0$), the sound comes from the right (left) side.

The schematic diagram of the proposed photonic SNN architecture is shown in Fig. 1(b), which is a fully connected network consisting of two PREs (PRE1 and PRE2) considered as the ear sensors, two POSTs (POST1 and POST2) for processing spikes and 2×2 synapses for the connection of two PREs and two POSTs. The difference between spike timings of the two POSTs ($\Delta t_o = t_{o2} - t_{o1}$) serves as the output of the network, providing information about sound azimuth. Because neurons and synapses of the brain process information through spikes, the two PREs in the proposed SNN form the encoding layer, converting input pulses into spikes with different spike timings. The VCSELs-SA are employed as the PREs and POSTs, producing spikes similar to LIF neurons. The PRE1 and PRE2 correspond to the right ear and left ear, respectively. When a PRE emits a spike, the spike is conveyed to the two POSTs through two synapses. Two PREs emit at various times ($\Delta t_i = t_{i2} - t_{i1} = t_L - t_R$) to simulate the ITD in the biologic network. In order to realize the sound azimuth detection function, similar to [21] and [51], the synaptic weight matrix is set to be diagonal, i.e. $\omega_{11} = \omega_{22}$, $\omega_{12} = \omega_{21}$, where ω_{io} denotes the connection weight between the i -th PRE and the o -th POST. In this way, the arrival

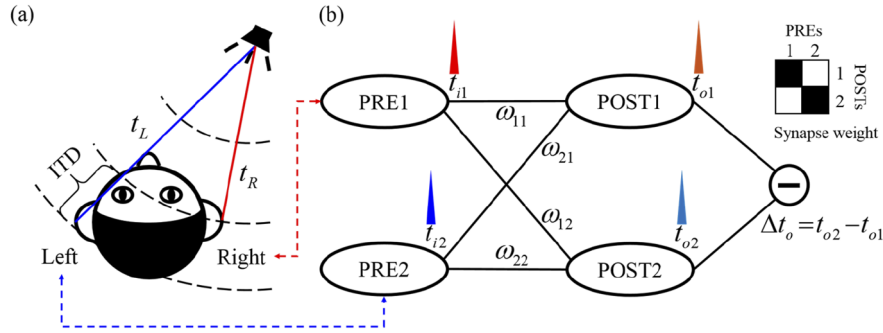


Fig. 1. Sound azimuth detection is emulated in a photonic SNN consisting of photonic neurons based on excitable VCSELs-SA. (a) Schematic diagram of the sound azimuth detection of the brain, where $ITD = t_L - t_R$ provides an estimate of the direction of sound propagation with respect to the listener. (b) Schematic structure of a 2×2 photonic SNN architecture to detect the sound azimuth from the $\Delta t_i = t_{i2} - t_{i1}$ (mimicking ITD) between the two PREs. The PRE1 and PRE2 correspond to the right ear and left ear (i.e., t_{i1} corresponds to t_R , and t_{i2} corresponds to t_L), respectively. The difference between the spike timings of the two POSTs ($\Delta t_o = t_{o2} - t_{o1}$) serves as the output of the network. The inset shows the map of synaptic weights in the 2×2 synapse matrix, which enables discrimination between different directions.

order of the two presynaptic spikes can be determined by the difference between spike timings of the two POSTs. Then, we can define Δt_o as an indication of the sound azimuth. Therefore, the purpose of the sound azimuth detection in this proposed photonic SNN is to identify Δt_o .

2.2. Rate equations of VCSELs-SA

The VCSEL-SA exhibiting excitable behavior similar to the LIF neuron is employed for all four neurons in the proposed photonic SNN. We extend the model of a solitary VCSEL-SA by adding terms accounting for the incoherent external input pulse injection. The rate equations of a VCSEL-SA as the PRE are written as follows [28,38,49]:

$$\frac{dS_i}{dt} = \Gamma_a g_a(n_{ia} - n_{0ia})S_i + \Gamma_s g_s(n_{is} - n_{0is})S_i - \frac{S_i}{\tau_{ph}} + \beta B_r n_{ia}^2 \quad (1)$$

$$\frac{dn_{ia}}{dt} = -\Gamma_a g_a(n_{ia} - n_{0ia})[S_i - k_e \frac{\tau_{ph}}{hc/\lambda_e} \frac{P_e(t, \Delta\tau)}{V_a}] - \frac{n_{ia}}{\tau_a} + \frac{I_a}{eV_a} \quad (2)$$

$$\frac{dn_{is}}{dt} = -\Gamma_s g_s(n_{is} - n_{0is})S_i - \frac{n_{is}}{\tau_s} + \frac{I_s}{eV_s} \quad (3)$$

Where the subscript i ($i = 1, 2$) denotes the serial number of the PREs. The subscripts a and s stand for the gain and absorber regions, respectively. $S_i(t)$ represents the photon density in the cavity, $n_a(t)$ ($n_s(t)$) is the carrier density in the gain (absorber) region. The term $k_e \tau_{ph} P_e(t, \Delta\tau) \lambda_e / hc V_a$ in Eq. (2) denotes the external input optical pulse, and $k_e (\Delta\tau)$ is the input strength (temporal duration). For simplicity, we consider $P_e = 1\text{mW}$, $\lambda_e = 845.58\text{nm}$. Specifically, V_a (V_s) is the gain (absorber) region cavity volume. Γ_a (Γ_s) is the gain (absorber) region confinement factor. g_a (g_s) is the gain (absorber) region differential gain/loss. τ_a (τ_s) is the gain (absorber) region carrier lifetime. n_{0a} (n_{0s}) is the gain (absorber) region transparency carrier density. I_a (I_s) is the bias current in the gain (absorber) region. Other parameters are the wavelength of VCSELs λ_i (850nm), the speed of light c , the spontaneous emission coupling factor β , the bimolecular recombination term B_r , the output power coupling coefficient η_c , and the photon lifetime τ_{ph} .

The output power of presynaptic VCSELs-SA can be expressed as Eq. (4).

$$P_i(t) \approx \frac{\eta_c \Gamma_a}{\tau_{ph}} \frac{hc}{\lambda_i} S_i(t) V_a \quad (4)$$

For the POSTs, Eq. (2) should be replaced as follows [28,38,49],

$$\frac{dn_{oa}}{dt} = -\Gamma_a g_a (n_{oa} - n_{0oa}) (S_o - \sum_{i=1}^2 \omega_{io} \frac{\tau_{ph}}{hc/\lambda_i} \frac{P_i(t-T)}{V_a}) - \frac{n_{oa}}{\tau_a} + \frac{I_a}{eV_a} \quad (5)$$

Where the subscript o ($o = 1, 2$) denotes the serial number of the POSTs. The term $\sum_{i=1}^2 \omega_{io} \tau_{ph} P_i(t-T) / hcV_a$ represents inputs of a POST, which are exactly the weighted sum of all the PREs with transmission delay $T = 3\text{ns}$. ω_{io} is the synaptic weight in the photonic SNN that can be adjusted. The rest equations and parameters are the same as those for the PREs.

For the simulation, we set typical parameters for all VCSELs-SA [38,49]: $h = 6.63 \times 10^{-34} \text{J} \cdot \text{s}$, $V_a = V_s = 2.4 \times 10^{-18} \text{m}^3$, $\Gamma_a = 0.06$, $\Gamma_s = 0.05$, $g_a = 2.9 \times 10^{-12} \text{m}^3 \text{s}^{-1}$, $g_s = 14.5 \times 10^{-12} \text{m}^3 \text{s}^{-1}$, $\tau_a = 1\text{ns}$, $\tau_s = 100\text{ps}$, $n_{0a} = 1.1 \times 10^{24} \text{m}^{-3}$, $n_{0s} = 0.89 \times 10^{24} \text{m}^{-3}$, $I_s = 0\text{mA}$, $\beta = 1 \times 10^{-4}$, $B_r = 10 \times 10^{-16} \text{m}^3 \text{s}^{-1}$, $\eta_c = 0.4$, $\tau_{ph} = 4.8\text{ps}$. With these parameters, we numerically solve the rate equations using the fourth-order Runge-Kutta method. The VCSEL-SA subject to optical pulse injection exhibits similar to the LIF neuron when it is biased below the threshold current ($I_{th} = 2.4\text{mA}$) [38]. Consequently, we consider $I_a = 2\text{mA}$ in the following analysis.

3. Properties of VCSEL-SA neurons

To begin with, we explore the **spike encoding property** of the PREs based on the excitability of VCSELs-SA. In a single presynaptic VCSEL-SA neuron, the input optical pulse is a rectangular shape, whose height and width are represented as the **input strength k_e** and the temporal duration $\Delta\tau$. Firstly, we fix the temporal duration at $\Delta\tau = 2\text{ns}$, and vary the input strength k_e . As depicted in Fig. 2(a), with the increase of k_e , the number of output spikes increases, and the time interval between the input pulse and the first output spike is smaller. Then, the input strength is kept constant at $k_e = 4 \times 10^3$, and $\Delta\tau$ is taken as the control variable. As shown in Fig. 2(b), increased $\Delta\tau$ leads to an increase in the number of output spikes. In addition, we find that the spike cannot be generated when k_e and $\Delta\tau$ are small. That means the excitability thresholds for the input strength and temporal duration exist in the spike encoding of VCSEL-SA neurons. For simplicity, we apply $k_e = 4 \times 10^3$, $\Delta\tau = 2\text{ns}$ to make both PREs emit a spike, unless otherwise stated.

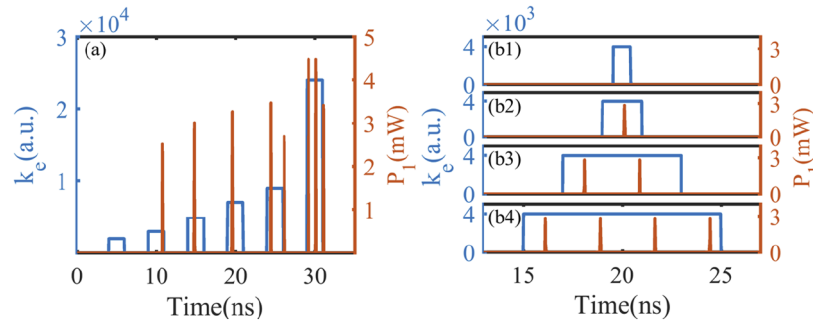


Fig. 2. Spike encoding property of the PREs subject to input optical pulses for different k_e and $\Delta\tau$. Optical pulse inputs (blue line) and corresponding spike outputs (orange line). (a) $k_e = 2 \times 10^3, 3 \times 10^3, 5 \times 10^3, 7 \times 10^3, 9 \times 10^3, 24 \times 10^3$, with $\Delta\tau = 2\text{ns}$. (b1, b2, b3, b4) $\Delta\tau = 0.9\text{ns}, 2\text{ns}, 6\text{ns}, 10\text{ns}$, with $k_e = 4 \times 10^3$.

In the proposed photonic SNN, each of the two POSTs is affected by the two presynaptic spikes. The role of POSTs is to process the encoded spikes generated by PREs by taking advantage of excitability of VCSEL-SA photonic neurons. Specifically, a simplified photonic SNN architecture is shown in Fig. 3(a). We take POST1 as an example to display the response process of the VCSEL-SA neuron in Fig. 3(b). Firstly, the POST1 integrates different encoded spikes generated by the two PREs in time as presented in Fig. 3(b1). Then the POST1 generates a sharp spike as displayed in Fig. 3(b3) once n_a of POST1 exceeds its excitability threshold as can be seen in Fig. 3(b2). That is to say, VCSEL-SA photonic neurons exhibit the excitability threshold response property, which is the basis for realization of sound azimuth detection.

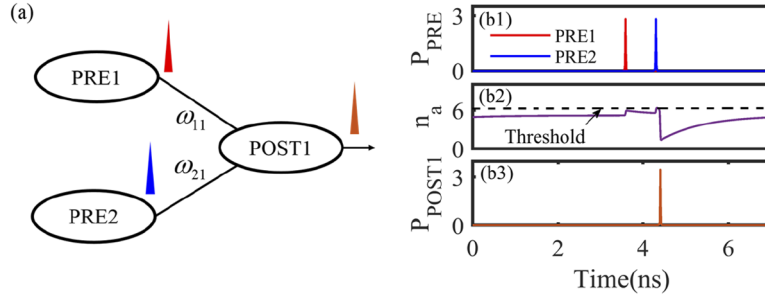


Fig. 3. (a) Schematic structure of a simplified photonic SNN architecture. (b) Schematic diagram of the response process of POST1 with $\omega_{11} = \omega_{21} = 5$. (b1) The power of encoded spikes generated by the two PREs, with $k_e = 4 \times 10^3$, $\Delta\tau = 2$ ns. (b2) The evolution of the carrier concentration in the gain section (n_a) of POST1. (b3) The output power of POST1.

4. Sound azimuth detection

Before we investigate the sound azimuth detection, we consider a simple case with a single PRE and a single POST, e.g., PRE1 and POST1, to explore the effect of synaptic weight ($\omega = \omega_{11}$) on the response property of the POST. The spike number as a function of ω is presented in Fig. 4(a). We set $k_e = 4 \times 10^3$, $\Delta\tau = 2$ ns, $I_a = 2$ mA. Here, the number ‘0’ indicates that the POST has no response, and the number ‘1’ indicates that the POST responds with a spike. It can be clearly seen that, when $\omega < 5.72$, the POST exhibits null response. The POST generates a spike when $\omega \geq 5.72$, since the weighted presynaptic spike energy is sufficiently strong to exceed the POST’s excitability threshold. Namely, the synapse weight threshold (ω_{th}) is 5.72. An example of the null response is shown in the inset (i) of Fig. 4(a) for $\omega = 5$. In the inset (ii) of Fig. 4(a), the POST responds a spike after the arrival of the presynaptic spike for $\omega = 10$. In addition, the effect of strength of input pulses (k_e) on the weight threshold (ω_{th}) is studied. It can be seen in Fig. 4(b) that ω_{th} decreases with the increase of k_e . This means that the presynaptic spike with a smaller k_e requires a larger weight to bring the POST to its excitability threshold.

In the following simulation, we consider that each of two weighted presynaptic spikes does not have enough energy to excite the POST, but their integrated sum possibly exceeds the POST’s excitability threshold to make the POST generate a spike. That is, both POSTs (POST1 and POST2) receiving two weighted presynaptic spikes have two kinds of responses, i.e., a null response and a spike. Therefore, the synapse weights below the threshold ($\omega < \omega_{th}$) are applied in our photonic SNN. Specifically, we use the synaptic weights in the range of 0 to 5.5 with two optical pulses of $k_e = 4 \times 10^3$, $\Delta\tau = 2$ ns in the following study.

The output of the proposed photonic SNN is based on spiking responses of the two POSTs with the diagonal weight setting. Although the two weighted presynaptic spikes are identical, the different arrival order of them will lead to different responses for the two POSTs. Hence, it is necessary to explore spiking responses of the two POSTs, which is useful for identifying the

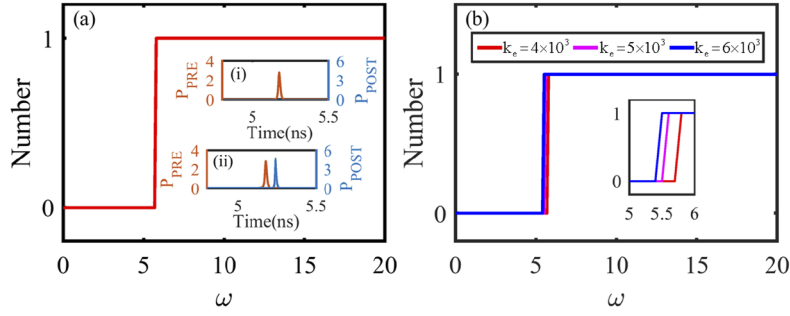


Fig. 4. (a) The spike number as a function of synaptic weight (ω). The inset (i) shows the null response of the POST for $\omega = 5$, and the inset (ii) shows that the POST responds a spike for $\omega = 10$, when a presynaptic spike is generated with $k_e = 4 \times 10^3$, $\Delta\tau = 2\text{ns}$, $I_a = 2\text{mA}$. (b) The spike number as a function of ω for different $k_e = 4 \times 10^3$, 5×10^3 , 6×10^3 , with $\Delta\tau = 2\text{ns}$.

available weight range contributing to the successful sound azimuth detection. As depicted in Fig. 5, two-dimensional maps in the parameter space of ω_{11} ($\omega_{22} = \omega_{11}$) and ω_{12} ($\omega_{21} = \omega_{12}$) for different Δt_i are plotted to illustrate spiking responses of the two POSTs, in which six cases are displayed in different colors. More precisely, the light blue region ('A') indicates that neither of two POSTs responds because the integrated total energy of the weighted presynaptic spikes is unable to excite a spike. The purple region ('B') indicates that POST2 responds with a spike, and POST1 has no response, while the red region ('F') is reversed. There are three color blocks showing that both POSTs generate a spike, which is dark blue ('E'), yellow ('C') and green ('D'). In this case, the integrated sum power of the weighted presynaptic spikes exceeds the excitability thresholds for the two POSTs. The dark blue region ('E') indicates that POST1 fires a spike earlier than POST2 ($\Delta t_o = t_{o2} - t_{o1} > 0$). The yellow region ('C') indicates that POST2 excites a spike prior to POST1 ($\Delta t_o < 0$). And the green region ('D') indicates that POST1 generates a spike at the same time as POST2 ($\Delta t_o = 0$). For the application of sound azimuth detection, the interested regions include dark blue region ('E') and yellow region ('C').

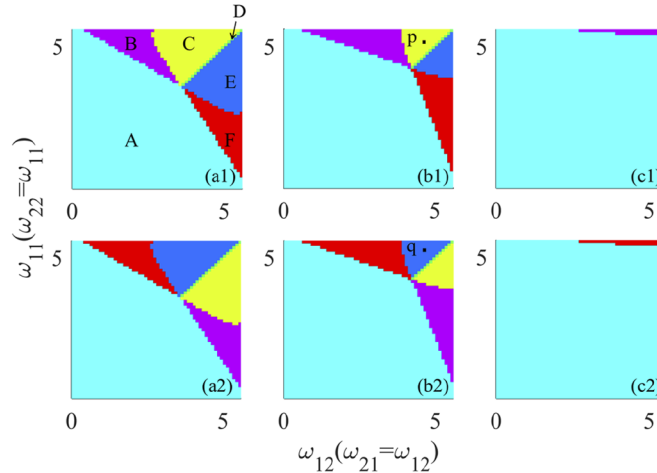


Fig. 5. Two-dimensional maps of spiking responses of the two POSTs in the parameter space of $\omega_{11}(\omega_{22} = \omega_{11})$ and $\omega_{12}(\omega_{21} = \omega_{12})$, with $k_e = 4 \times 10^3$, $\Delta\tau = 2\text{ns}$, (a1, b1, c1) for $\Delta t_i = t_{i2} - t_{i1} = 0.5\text{ns}$, 1ns , 2.5ns , (a2, b2, c2) for $\Delta t_i = t_{i2} - t_{i1} = -0.5\text{ns}$, -1ns , -2.5ns .

In Figs. 5(a1), (b1), and (c1), PRE1 emits a spike earlier than PRE2 ($\Delta t_i = t_{i2} - t_{i1} = 0.5\text{ns}, 1\text{ns}, 2.5\text{ns}$), but in Figs. 5(a2), (b2), and (c2), PRE2 emits a spike earlier than PRE1 ($\Delta t_i = t_{i2} - t_{i1} = -0.5\text{ns}, -1\text{ns}, -2.5\text{ns}$). We observe that spiking responses of POSTs are distinct for different values of $\Delta t_i > 0$ (or $\Delta t_i < 0$), which can be used to mimic the sound azimuth detection of the brain. Here, the Δt_o serves as an indication of the sound azimuth, that is, the weight ranges used for sound localization are dark blue ('E') and yellow ('C') regions. Compared the top row with the bottom row of Fig. 5, the yellow region and the dark blue region are completely symmetrical, proving that for a set of determined weights, the positive and negative value of Δt_i can be determined by Δt_o . Figure 5 also shows that as Δt_i increases (from Fig. 5(a) to Fig. 5(c)), the region where both POSTs generate a spike, including the dark blue and yellow regions, decreases gradually until disappears. This indicates that the range of available weights leading to the successful sound azimuth detection reduces with the increment of Δt_i . We have also considered some other cases of Δt_i . It is found that, when $\Delta t_i \leq -3.2\text{ns}$ and $\Delta t_i \geq 3.2\text{ns}$, the temporal integration of spikes has no effect, so the region where both POSTs generate a spike no longer exists.

Specifically, we select a set of weights corresponding to the points 'p' and 'q' in Fig. 5(b) to illustrate the implementation of sound localization function, that is, $\omega_{11} = \omega_{22} = 5.2$, $\omega_{12} = \omega_{21} = 4.6$. The schematic illustration of the implementation of sound azimuth detection is shown in Fig. 6(a) and Fig. 6(b), where the time difference of two presynaptic spikes is $\Delta t_i = 1\text{ns}$ (corresponding to right/left pattern) and $\Delta t_i = -1\text{ns}$ (corresponding to left/right pattern), respectively. In Fig. 6(a), the negative Δt_o ($\Delta t_o < 0$) responds to the right/left pattern, that is, the sound reaches the PRE1 (right ear) first ($\Delta t_i > 0$). While in Fig. 6(b), the positive Δt_o ($\Delta t_o > 0$) reveals that the sound is from the PRE2 (left) side ($\Delta t_i < 0$), which responds to the left/right pattern. Therefore, the photonic SNN successfully mimics the sound azimuth detection of the brain, in which the arrival order of two PRE spikes is accurately discriminated by the spike timing difference of two POST spikes.

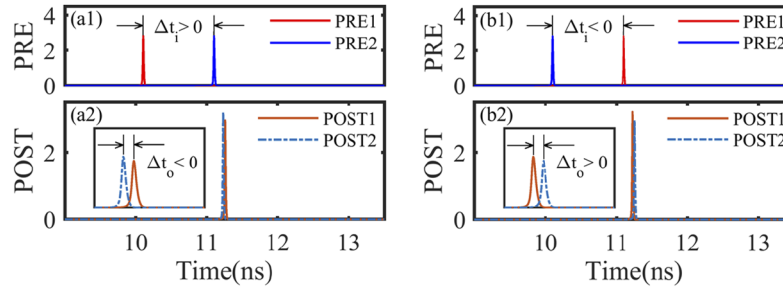


Fig. 6. Schematic illustration of sound azimuth detection performed by the proposed photonic SNN. (a) Responses of POST1 and POST2 when PRE1 arrives earlier than PRE2 ($\Delta t_i = t_{i2} - t_{i1} = 1\text{ns}$). The inset which is the enlarged (a2) shows the output of the SNN $\Delta t_o = t_{o2} - t_{o1} < 0$. (b) Responses of POST1 and POST2 when PRE2 arrives earlier than PRE1 ($\Delta t_i = t_{i2} - t_{i1} = -1\text{ns}$). The inset which is the enlarged (b2) shows the output of the SNN $\Delta t_o = t_{o2} - t_{o1} > 0$. The synapse weights keep constant, which are $\omega_{11} = \omega_{22} = 5.2$, $\omega_{12} = \omega_{21} = 4.6$.

Note that, the range of the ITD for the human ears is typically in the range of -0.6ms to 0.6ms [21]. To explore the effective detection range of Δt_i in which the sound direction can be correctly identified in our proposed photonic SNN, we further consider the dependence of Δt_o on Δt_i . Figure 7 shows the Δt_o as a function of the Δt_i (mimicking ITD). Figure 7(a) compares the effective detection range under three sets of weight values. For $\omega_{11} = \omega_{22} = 5.2$, $\omega_{12} = \omega_{21} = 4.6$ (red curve), the effective detection range is from -1.5ns to 1.5ns . For $\omega_{11} = \omega_{22} = 5.2$, $\omega_{12} = \omega_{21} = 4.3$ (blue curve), the effective detection range is from -1.26ns

to 1.26ns. For $\omega_{11} = \omega_{22} = 5.2$, $\omega_{12} = \omega_{21} = 4.0$ (orange curve), the effective detection range is from -1.0ns to 1.0ns . Compared with human ears, our model has a higher resolution, since the effective detection range is only several nanoseconds. In accordance with Fig. 4(b), we also discuss the effect of input strength (k_e) on the effective detection range in Fig. 7(b), in which $\omega_{11} = \omega_{22} = 5.2$, $\omega_{12} = \omega_{21} = 4.6$. We can observe that with the increase of k_e , the effective detection range becomes wider. Besides, the effect of different bias currents I_a of VCSELs-SA on the effective detection range is illustrated in Fig. 7(c). Here, the bias currents of four neurons are set to be identical and the values of I_a are 1.97mA, 2.0mA, and 2.02mA, respectively. It is found that the effective detection range becomes wide as I_a increases. In addition, the spontaneous emission coupling factor is set to be $\beta = 1 \times 10^{-4}$ for all neurons in above simulations. We performed some simulations similar to Fig. 6 for different values of β and found that the sound azimuth detection cannot be realized when the value of β is higher than 1×10^{-4} . As shown in Fig. 7(d), we further analyze the effect of the spontaneous emission noise in VCSELs-SA on the effective detection range. It is shown that the effective detection range becomes narrow with the decrease of β . The sound direction calculated in Fig. 7 is consistent with the result demonstrated in Fig. 6, that is, the sound coming from the right side ($\Delta t_i > 0$) corresponds to $\Delta t_o < 0$, and the sound coming from the left side ($\Delta t_i < 0$) corresponds to $\Delta t_o > 0$. Thus, the sound azimuth can be evaluated by the value of Δt_o , and the effective detection range also can be measured.

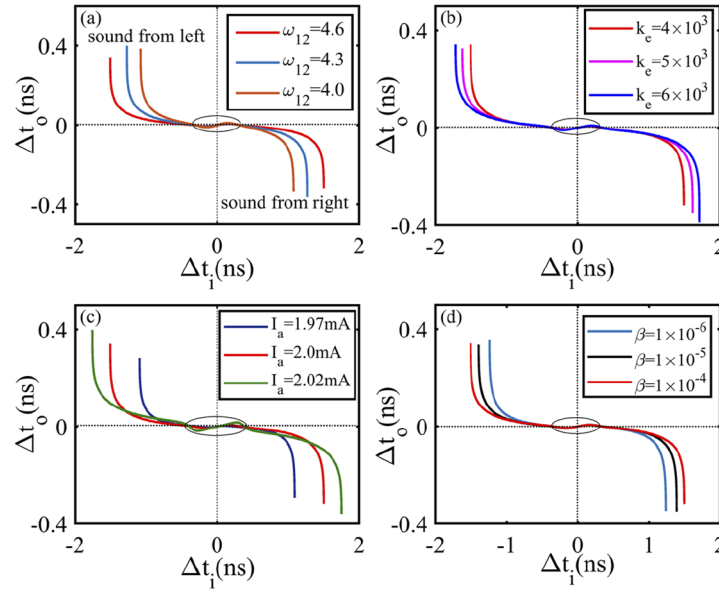


Fig. 7. The calculated Δt_o as a function of the Δt_i (mimicking ITD) for (a) $\omega_{12} = \omega_{21} = 4.6, 4.3, 4.0$, with $\omega_{11} = \omega_{22} = 5.2$, $k_e = 4 \times 10^3$, $\Delta\tau = 2\text{ns}$, (b) $k_e = 4 \times 10^3, 5 \times 10^3, 6 \times 10^3$ with $\omega_{11} = \omega_{22} = 5.2$, $\omega_{12} = \omega_{21} = 4.6$, $\Delta\tau = 2\text{ns}$, (c) $I_a = 1.97\text{mA}, 2.0\text{mA}, 2.02\text{mA}$ with $\omega_{11} = \omega_{22} = 5.2$, $\omega_{12} = \omega_{21} = 4.6$, $k_e = 4 \times 10^3$, $\Delta\tau = 2\text{ns}$, (d) $\beta = 1 \times 10^{-4}, 1 \times 10^{-5}, 1 \times 10^{-6}$ with $\omega_{11} = \omega_{22} = 5.2$, $\omega_{12} = \omega_{21} = 4.6$, $k_e = 4 \times 10^3$, $\Delta\tau = 2\text{ns}$.

In addition, we note that near $\Delta t_i = 0\text{ns}$ (as labeled by black circles) in Fig. 7, the variation tendency of Δt_o is different from that previously demonstrated. We further discuss the spiking responses of two POSTs in two-dimensional maps with several smaller Δt_i ($\Delta t_i = 0.1\text{ns}, 0.2\text{ns}, 0.3\text{ns}$) as shown in Fig. 8. Compared with Fig. 5, the distribution of yellow and dark blue regions, which are used for sound azimuth detection, is more complex, but still behaves a certain regularity. When the Δt_i is relatively small, i.e., the spike timing of PRE1 is very close to that of PRE2, the

Δt_o is more sensitive to synaptic weights. Hence, to obtain robust sound azimuth detection, a larger Δt_i is suggested.

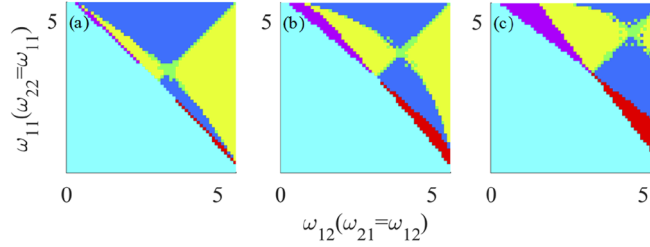


Fig. 8. Two-dimensional maps of spiking responses of the two POSTs in the parameter space of $\omega_{11}(\omega_{22} = \omega_{11})$ and $\omega_{12}(\omega_{21} = \omega_{12})$, for (a) $\Delta t_i = 0.1\text{ns}$, (b) $\Delta t_i = 0.2\text{ns}$, (c) $\Delta t_i = 0.3\text{ns}$, with $k_e = 4 \times 10^3$, $\Delta\tau = 2\text{ns}$.

Note, the intrinsic device-to-device variation of the photonic neurons may exist in the proposed photonic SNN system implementation. Hence, the effect of device variations on the implementation of sound localization function deserves further consideration. To this end, some random noises are introduced for the bias currents in the gain region I_a of VCSELs-SA. Similar to Fig. 6, we perform the sound azimuth detection function with the bias currents of four neurons added some random noises and other conditions remaining unchanged. In Fig. 6, the bias currents of PRE1, PRE2, POST1 and POST2 are equal to $I_a = 2\text{mA}$. Here, we consider a practical condition that the bias currents of PRE1, PRE2, POST1 and POST2 are $I_{a1}' = 2.01\text{mA}$, $I_{a2}' = 1.99\text{mA}$, $I_{a3}' = 2.02\text{mA}$ and $I_{a4}' = 2.0\text{mA}$, respectively. As shown in Fig. 9, the negative (positive) Δt_o responds to the right/left (left/right) pattern, indicating that the sound azimuth detection can still be successfully implemented even with slight bias current fluctuations. We have also considered some other cases of bias current fluctuations and obtained similar results (not shown here). Therefore, our proposed photonic SNN is robust to the bias current variations of VCSELs-SA to some extent, which benefits the practical implementation of the photonic sound azimuth detection function.

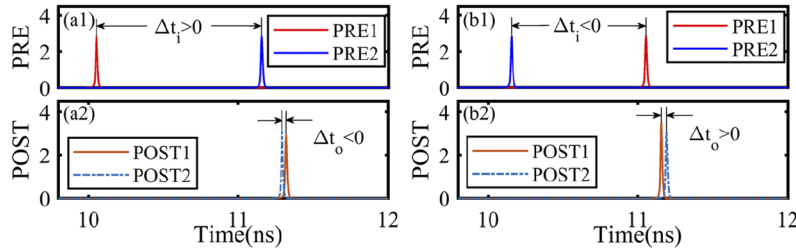


Fig. 9. The same as in Fig. 6, but the bias currents of PRE1, PRE2, POST1 and POST2 are $I_{a1}' = 2.01\text{mA}$, $I_{a2}' = 1.99\text{mA}$, $I_{a3}' = 2.02\text{mA}$ and $I_{a4}' = 2.0\text{mA}$, respectively.

Without loss of generality, we further consider the case of the transmission delay mismatch which refers to there are subtle differences among four transmission delays. As presented in Fig. 10, the transmission delays are $T_{11}' = 3.01\text{ns}$, $T_{12}' = 3.02\text{ns}$, $T_{21}' = 2.99\text{ns}$ and $T_{22}' = 2.98\text{ns}$, respectively. The result in Fig. 10 which is similar to Fig. 6 indicates that the sound azimuth detection is still successfully realized when four transmission delays have subtle differences. Some other cases of the transmission delay mismatch are also taken into account, and similar results are achieved (not shown here). Consequently, the small transmission delay mismatch is

allowed in the realization of the sound azimuth detection, which is favorable to the practical construction of the proposed photonic SNN.

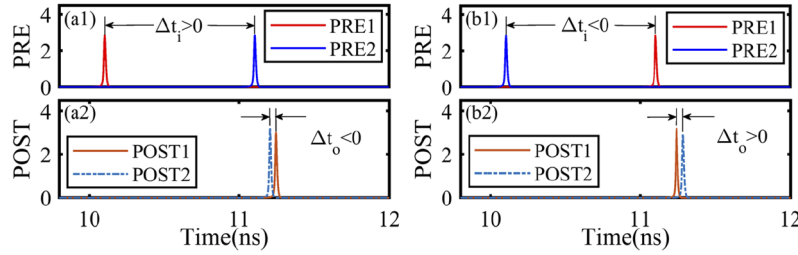


Fig. 10. The same as in Fig. 6, but the transmission delays are $T_{11}' = 3.01$ ns, $T_{12}' = 3.02$ ns, $T_{21}' = 2.99$ ns and $T_{22}' = 2.98$ ns, respectively.

5. Conclusion

In summary, we propose a photonic SNN based on excitable VCSELs-SA successfully mimicking the sound azimuth detection function of the brain for the first time. In this photonic SNN, the PREs employ the spike encoding property of VCSELs-SA to convert input pulses into spikes. The POSTs process presynaptic spikes by utilizing the threshold response properties of VCSELs-SA. We reveal that the difference between the precise spike timing of the two POSTs can be used as an indication of the sound azimuth. For instance, for $\omega_{11} = \omega_{22} > \omega_{12} = \omega_{21}$, the negative Δt_o responds to the right/left pattern, and the positive Δt_o responds to the left/right pattern. Moreover, the range of weights contributing to the successful sound azimuth detection is identified, which provides theoretical guidelines for designing photonic SNN for sound localization. Compared with the biological sound localization system, the photonic SNN has comparable low energy consumption and higher resolution. More specifically, the effective detection range of time interval between two presynaptic spikes in the proposed photonic SNN is similar to that of the biological auditory system, but with a much higher resolution which is at the nanosecond time scale. The numerical simulations further indicate that the photonic sound azimuth detection is immune to small device variations. Therefore, we demonstrate that the SNN is biologically plausible and feasible for sound azimuth detection. In conclusion, to the best of our knowledge, this work is the first step forward in enabling the photonic SNN to process more complex brain-inspired spiking information.

Funding

National Natural Science Foundation of China (61974177, 61674119); National Postdoctoral Program for Innovative Talents (BX201600118); China Postdoctoral Science Foundation (2017M613072); Shaanxi Province Postdoctoral Science Foundation.

Acknowledgments

This work was supported in part by the National Natural Science Foundation of China (Grants 61974177, 61674119), the Postdoctoral innovation talent program in China (Grant BX201600118), the project funded by China Postdoctoral Science Foundation (Grant 2017M613072), Postdoctoral Science Foundation in Shaanxi Province of China.

Disclosures

The authors declare no conflicts of interest.

References

1. D. A. Drachman, "Do we have brain to spare?" *Neurology* **64**(12), 2004–2005 (2005).
2. V. M. Ho, J. A. Lee, and K. C. Martin, "The cell biology of synaptic plasticity," *Science* **334**(6056), 623–628 (2011).
3. I. A. Basheer and M. Hajmeer, "Artificial neural networks: fundamentals, computing, design, and application," *J. Microbiol. Methods* **43**(1), 3–31 (2000).
4. W. Maass, "Networks of spiking neurons: The third generation of neural network models," *Neural Netw.* **10**(9), 1659–1671 (1997).
5. S. Ghosh-Dastidar and H. Adeli, "Spiking neural networks," *Int. J. Neur. Syst.* **19**(04), 295–308 (2009).
6. E. M. Izhikevich, "Which model to use for cortical spiking neurons?" *IEEE Trans. Neural Netw.* **15**(5), 1063–1070 (2004).
7. C. Mead, "Neuromorphic electronic systems," *Proc. IEEE* **78**(10), 1629–1636 (1990).
8. G. Indiveri, B. Linares-Barranco, T. J. Hamilton, A. van Schaik, R. Etienne-Cummings, T. Delbruck, S.-C. Liu, P. Dudek, P. Häfliger, S. Renaud, J. Schemmel, G. Cauwenberghs, J. Arthur, K. Hynna, F. Folowosele, S. Saighi, T. Serrano-Gotarredona, J. Wijekoon, Y. Wang, and K. Boahen, "Neuromorphic silicon neuron circuits," *Front. Neurosci.* **5**, 73 (2011).
9. E. Painkras, L. A. Plana, J. Garside, S. Temple, F. Galluppi, C. Patterson, D. R. Lester, A. D. Brown, and S. B. Furber, "Spinnaker: A 1-W 18-core system-on-chip for massively-parallel neural network simulation," *IEEE J. Solid-State Circuits* **48**(8), 1943–1953 (2013).
10. B. V. Benjamin, P. Gao, E. McQuinn, S. Choudhary, A. R. Chandrasekaran, J.-M. Bussat, R. Alvarez-Icaza, J. V. Arthur, P. A. Merolla, and K. Boahen, "Neurogrid: A mixed-analog-digital multichip system for large-scale neural simulations," *Proc. IEEE* **102**(5), 699–716 (2014).
11. S. B. Furber, F. Galluppi, S. Temple, and L. A. Plana, "The SpiNNaker project," *Proc. IEEE* **102**(5), 652–665 (2014).
12. P. A. Merolla, J. V. Arthur, R. Alvarez-Icaza, A. S. Cassidy, J. Sawada, F. Akopyan, B. L. Jackson, N. Imam, C. Guo, Y. Nakamura, B. Brezzo, I. Vo, S. K. Esser, R. Appuswamy, B. Taba, A. Amir, M. D. Flickner, W. P. Risk, R. Manohar, and D. S. Modha, "A million spiking-neuron integrated circuit with a scalable communication network and interface," *Science* **345**(6197), 668–673 (2014).
13. M. Prezioso, F. Merrih-Bayat, B. D. Hoskins, G. C. Adam, K. K. Likharev, and D. B. Strukov, "Training and operation of an integrated neuromorphic network based on metal-oxide memristors," *Nature* **521**(7550), 61–64 (2015).
14. S. Park, M. Chu, J. Kim, J. Noh, M. Jeon, B. H. Lee, H. Hwang, B. Lee, and B.-G. Lee, "Electronic system with memristive synapses for pattern recognition," *Sci. Rep.* **5**(1), 10123 (2015).
15. R. A. Nawrocki, R. M. Voyles, and S. E. Shaheen, "A mini review of neuromorphic architectures and implementations," *IEEE Trans. Electron Devices* **63**(10), 3819–3829 (2016).
16. J. Shen, D. Ma, Z. Gu, M. Zhang, X. Zhu, X. Xu, Q. Xu, Y. Shen, and G. Pan, "Darwin: a neuromorphic hardware co-processor based on spiking neural networks," *Sci. China Inf. Sci.* **59**(2), 1–5 (2016).
17. P. Yao, H. Wu, B. Gao, S. B. Eryilmaz, X. Huang, W. Zhang, Q. Zhang, N. Deng, L. Shi, H.-S. P. Wong, and H. Qian, "Face classification using electronic synapses," *Nat. Commun.* **8**(1), 15199 (2017).
18. C. D. Schuman, T. E. Potok, R. M. Patton, J. D. Birdwell, M. E. Dean, G. S. Rose, and J. S. Plank, "A survey of neuromorphic computing and neural networks in hardware," arXiv preprint arXiv:1705.06963 (2017).
19. C. Li, D. Belkin, Y. Li, P. Yan, M. Hu, N. Ge, H. Jiang, E. Montgomery, P. Lin, Z. Wang, W. Song, J. P. Strachan, M. Barnell, Q. Wu, R. S. Williams, J. J. Yang, and Q. Xia, "Efficient and self-adaptive in-situ learning in multilayer memristor neural networks," *Nat. Commun.* **9**(1), 2385 (2018).
20. I. Boybat, M. L. Gallo, S. R. Nandakumar, T. Moraitis, T. Parnell, T. Tuma, B. Rajendran, Y. Leblebici, A. Sebastian, and E. Eleftheriou, "Neuromorphic computing with multi-memristive synapses," *Nat. Commun.* **9**(1), 2514 (2018).
21. W. Wang, G. Pedretti, V. Milo, R. Carboni, A. Calderoni, N. Ramaswamy, A. S. Spinelli, and D. Ielmini, "Learning of spatiotemporal patterns in a spiking neural network with resistive switching synapses," *Sci. Adv.* **4**(9), eaat4752 (2018).
22. W. Wang, G. Pedretti, V. Milo, R. Carboni, A. Calderoni, N. Ramaswamy, A. S. Spinelli, and D. Ielmini, "Computing of temporal information in spiking neural networks with ReRAM synapses," *Faraday Discuss.* **213**, 453–469 (2019).
23. S. G. Hu, G. C. Qiao, Y. A. Liu, L. M. Rong, Q. Yu, and Y. Liu, "An improved memristor model connecting plastic synapse and nonlinear spiking neuron," *J. Phys. D: Appl. Phys.* **52**(27), 275402 (2019).
24. A. Hurtado, I. D. Henning, and M. J. Adams, "Optical neuron using polarization switching in a 1550 nm-VCSEL," *Opt. Express* **18**(24), 25170–25176 (2010).
25. W. Coomans, L. Gelens, S. Beri, J. Danckaert, and G. Van der Sande, "Solitary and coupled semiconductor ring lasers as optical spiking neurons," *Phys. Rev. E* **84**(3), 036209 (2011).
26. A. Hurtado, K. Schires, I. D. Henning, and M. J. Adams, "Investigation of vertical cavity surface emitting laser dynamics for neuromorphic photonic systems," *Appl. Phys. Lett.* **100**(10), 103703 (2012).
27. T. Van Vaerenbergh, M. Fiers, P. Mechet, T. Spuesens, R. Kumar, G. Morthier, B. Schrauwen, J. Dambre, and P. Bienstman, "Cascadable excitability in microrings," *Opt. Express* **20**(18), 20292–20308 (2012).
28. M. A. Nahmias, B. J. Shastri, A. N. Tait, and P. R. Prucnal, "A leaky integrate-and-fire laser neuron for ultrafast cognitive computing," *IEEE J. Sel. Top. Quantum Electron.* **19**(5), 1–12 (2013).
29. F. Selmi, R. Braive, G. Beaudoin, I. Sagnes, R. Kuszelewicz, and S. Barbay, "Relative refractory period in an excitable semiconductor laser," *Phys. Rev. Lett.* **112**(18), 183902 (2014).

30. B. J. Shastri, M. A. Nahmias, A. N. Tait, A. W. Rodriguez, B. Wu, and P. R. Prucnal, "Spike processing with a graphene excitable laser," *Sci. Rep.* **6**(1), 19126 (2016).
31. B. Romeira, R. Avo, J. M. L. Figueiredo, S. Barland, and J. Javaloyes, "Regenerative memory in time-delayed neuromorphic photonic resonators," *Sci. Rep.* **6**(1), 19510 (2016).
32. P. R. Prucnal, B. J. Shastri, T. F. De Lima, M. A. Nahmias, and A. N. Tait, "Recent progress in semiconductor excitable lasers for photonic spike processing," *Adv. Opt. Photonics* **8**(2), 228–299 (2016).
33. S. Y. Xiang, Y. H. Zhang, X. X. Guo, J. F. Li, A. J. Wen, W. Pan, and Y. Hao, "Cascadable neuron-like spiking dynamics in coupled VCSELs subject to orthogonally polarized optical pulse injection," *IEEE J. Sel. Top. Quantum Electron.* **23**(6), 1–7 (2017).
34. T. Deng, J. Robertson, and A. Hurtado, "Controlled propagation of spiking dynamics in vertical-cavity surface-emitting lasers: towards neuromorphic photonic networks," *IEEE J. Sel. Top. Quantum Electron.* **23**(6), 1–8 (2017).
35. J. Robertson, T. Deng, J. Javaloyes, and A. Hurtado, "Controlled inhibition of spiking dynamics in VCSELs for neuromorphic photonics: theory and experiments," *Opt. Lett.* **42**(8), 1560–1563 (2017).
36. J. Robertson, E. Wade, Y. Kopp, J. Bueno, and A. Hurtado, "Toward neuromorphic photonic networks of ultrafast spiking laser neurons," *IEEE J. Sel. Top. Quantum Electron.* **26**(1), 1–15 (2020).
37. S. Y. Xiang, Y. H. Zhang, X. X. Guo, A. J. Wen, and Y. Hao, "Photonic generation of neuron-like dynamics using VCSELs subject to double polarized optical injection," *J. Lightwave Technol.* **36**(19), 4227–4234 (2018).
38. Y. H. Zhang, S. Y. Xiang, J. K. Gong, X. X. Guo, A. J. Wen, and Y. Hao, "Spike encoding and storage properties in mutually coupled vertical-cavity surface-emitting lasers subject to optical pulse injection," *Appl. Opt.* **57**(7), 1731–1737 (2018).
39. Y. H. Zhang, S. Y. Xiang, X. X. Guo, A. J. Wen, and Y. Hao, "Polarization-resolved and polarization-multiplexed spike encoding properties in photonic neuron based on VCSEL-SA," *Sci. Rep.* **8**(1), 16095 (2018).
40. Y. H. Zhang, S. Y. Xiang, X. X. Guo, A. J. Wen, and Y. Hao, "All-optical inhibitory dynamics in photonic neuron based on polarization mode competition in a VCSEL with an embedded saturable absorber," *Opt. Lett.* **44**(7), 1548–1551 (2019).
41. M. P. Fok, Y. Tian, D. Rosenbluth, and P. R. Prucnal, "Pulse lead/lag timing detection for adaptive feedback and control based on optical spike-timing-dependent plasticity," *Opt. Lett.* **38**(4), 419–421 (2013).
42. R. Toole and M. P. Fok, "Photonic implementation of a neuronal algorithm applicable towards angle of arrival detection and localization," *Opt. Express* **23**(12), 16133–16141 (2015).
43. Q. Ren, Y. Zhang, R. Wang, and J. Zhao, "Optical spike-timing-dependent plasticity with weight-dependent learning window and reward modulation," *Opt. Express* **23**(19), 25247–25258 (2015).
44. B. Gholipour, P. Bastock, C. Craig, K. Khan, D. Hewak, and C. Soci, "Amorphous metal-sulphide microfibers enable photonic synapses for brain-like computing," *Adv. Opt. Mater.* **3**(5), 635–641 (2015).
45. R. Toole, A. N. Tait, T. F. De Lima, M. A. Nahmias, B. J. Shastri, P. R. Prucnal, and M. P. Fok, "Photonic implementation of spike-timing-dependent plasticity and learning algorithms of biological neural systems," *J. Lightwave Technol.* **34**(2), 470–476 (2016).
46. Q. Li, Z. Wang, Y. Le, C. Sun, X. Song, and C. Wu, "Optical implementation of neural learning algorithms based on cross-gain modulation in a semiconductor optical amplifier," *Proc. SPIE* **10019**, 100190E (2016).
47. Z. Cheng, C. Ríos, W. H. P. Pernice, C. D. Wright, and H. Bhaskaran, "On-chip photonic synapse," *Sci. Adv.* **3**(9), e1700160 (2017).
48. S. Y. Xiang, J. K. Gong, Y. H. Zhang, X. X. Guo, Y. N. Han, A. J. Wen, and Y. Hao, "Numerical implementation of wavelength-dependent photonic spike timing dependent plasticity based on VCSOA," *IEEE J. Quantum Electron.* **54**(6), 1–7 (2018).
49. S. Y. Xiang, Y. H. Zhang, J. K. Gong, X. X. Guo, L. Lin, and Y. Hao, "STDP-based unsupervised spike pattern learning in a photonic spiking neural network with VCSELs and VCSOAs," *IEEE J. Sel. Top. Quantum Electron.* **25**(6), 1–9 (2019).
50. D. McAlpine and B. Grothe, "Sound localization and delay lines-do mammals fit the model?," *Trends Neurosci.* **26**(7), 347–350 (2003).
51. Y. He, S. Nie, R. Liu, S. Jiang, Y. Shi, and Q. Wan, "Spatiotemporal information processing emulated by multiterminal neuro-transistor networks," *Adv. Mater.* **31**(21), 1900903 (2019).
52. M. Häusser, "The Hodgkin-Huxley theory of the action potential," *Nat. Neurosci.* **3**(S11), 1165 (2000).
53. J. Bono and C. Clopath, "Modeling somatic and dendritic spike mediated plasticity at the single neuron and network level," *Nat. Commun.* **8**(1), 706 (2017).
54. D. F. M. Goodman and R. Brette, "Spike-timing-based computation in sound localization," *PLoS Comput. Biol.* **6**(11), e1000993 (2010).
55. K. E. Hancock and B. Delgutte, "A physiologically based model of interaural time difference discrimination," *J. Neurosci.* **24**(32), 7110–7117 (2004).